Germanium Vacancies and Charge Transport Properties in $Ba_8Zn_xGe_{46-x-y}\square_y$

E. Alleno,* G. Maillet, O. Rouleau, E. Leroy, and C. Godart

ICMPE- CMTR, CNRS-UMR 7182, 2-8, rue H. Dunant, 94320 Thiais, France

W. Carrillo-Cabrera, P. Simon, and Yu. Grin

Max Planck Institut für Chemische Physik fester Stoffe, Nöthnitzer Strasse 40, 01187, Dresden, Germany

Received October 21, 2008. Revised Manuscript Received February 13, 2009

The $Ba_8Zn_xGe_{46-x-y}\square_y$ ($4 \le x \le 8$, $\square$ = Ge vacancy) solid solution crystallizes in the clathrate type I structure as indicated by X-ray powder diffraction and transmission electron microscopy. The fraction of vacancies (y) derived from electron probe microanalysis varies like $y = 3.3 - 0.54x$ for $0 \le x \le 6$ and $y = 0$ for $6 < x \le 8$. A simplified band picture can explain how the ratio (2−)/(4−) of formal oxidation numbers of zinc and of vacancy leads to the ∼1/2 slope of the $y = f(x)$ relation. Hall effect measurements indicate that the $Ba_8Zn_xGe_{46-x-y}\square_y$ definitely deviate from the Zintl rule when $0 \le x < 4$, weakly deviate from the the Zintl rule when $4 \le x \le 6$, and fulfill the Zintl rule when $6 < x \le 8$. Resistivity versus temperature data for $4 \le x \le 8$ are in line with a "bad metal" behavior ($x \sim 4$) evolving toward a degenerate semiconducting behavior ($x \sim 8$). The Seebeck coefficient increases with x in agreement with the charge carrier concentration variation and reaches −67.1 μV/K in $Ba_{7.95}Zn_{7.83}Ge_{38.17}$ which also displays the largest power factor (PF = 3.75 $\mu W \cdot K^{-2} \cdot cm^{-1}$ at 300 K) in this series.

Introduction

Type I inorganic clathrates $A_8M_xX_{46-x-y}\square_y$ ($\square$ = X vacancy) are compounds built by group IV elements (X), partially substituted by group VIII, IB, IIB, or IIIA elements (M), which form large cages filled by electropositive group IIA elements (A).[1−3] The compounds with M = Ga and X = Ge attracted great interest because of their potential for thermoelectricity generation.[4−7] The $A_8Ga_xGe_{46-x-y}\square_y$ compounds crystallize in the type I clathrate structure (Na_8Si_{46} structure type, cubic lattice, space group $Pm\bar{3}n$). The Ga/Ge atoms are four-bonded (4b) like in elemental germanium and form large 20-atom cages (pentagonal dodecahedron) and 24-atom cages (tetrakaidecahedron) which share their faces to build a three-dimensional network.[8] The existence of vacancies in the MX network of type I clathrate was initially shown in $K_8Ge_{44}\square_2$,[9] in $Cs_8Sn_{44}\square_2$,[10,11] in $Rb_8Sn_{44}\square_2$,[12] and more recently in $Ba_8Ge_{43}\square_3$[13−15] and in $Ba_8Ga_xGe_{46-x-y}\square_y$.[16,17] In the generic clathrate type I structure presented in Figure 1, two of the eight alkaline-earth atoms per formula unit fill the 20-atom cages while the six remaining ones fill the 24-atom cages. In the larger 24-atom cage, the A atom displays large and localized vibrations[18,19] ($\langle u \rangle \sim 0.18$ Å at 300 K in $Sr_8Ga_{16}Ge_{30}$) which are thought to resonantly scatter the heat-carrying phonons and strongly reduce the lattice thermal conductivity to values as low as 1 $W \cdot m^{-1} \cdot K^{-1}$ at 300 K,[4] that is, smaller than the value found in amorphous SiO_2 (1.2 $W \cdot m^{-1} \cdot K^{-1}$). Thus, the low thermal conductivity (lattice + charge carrier contributions ∼ 2 $W \cdot m^{-1} \cdot K^{-1}$ at 300 K) necessary for good thermoelectric performances is a general feature of the type I clathrates. Despite their "amorphous-like" lattice thermal conductivity, the $A_8Ga_{16}Ge_{30}$ compounds exhibit Seebeck coefficients (α) and electrical resistivity (ρ)

* Corresponding author. E-mail: eric.alleno@icmpe.cnrs.fr.

(1) Eisenmann, B.; Schäfer, H.; Zagler, R. *J. Less-Common Met.* **1986**, *118*, 43.
(2) Cordier, G.; Woll, P. *J. Less-Common Met.* **1991**, *169*, 291.
(3) Czybulka, A.; Kuhl, B.; Schuster, H. U. *Z. Anorg. Allg. Chem.* **1991**, *594*, 23.
(4) Nolas, G. S.; Cohn, J. L.; Slack, G. A.; Schujman, S. B. *Appl. Phys. Lett.* **1998**, *73*, 178.
(5) Saramat, A.; Svensson, G.; Palmqvist, A. E. C.; Stiewe, C.; Mueller, E.; Platzek, D.; Williams, S. G. K.; Rowe, D. M.; Bryan, J. D.; Stucky, G. D. *J. Appl. Phys.* **2006**, *99*, 023708.
(6) Anno, H.; Hokazono, M.; Kawamura, M.; Nagao, J.; Matsubara, K. *Proceedings of the 21st International Conference on Thermoelectrics*, Long Beach, CA, U.S.A., Aug 25−29, 2002; IEEE: Piscataway, NJ, 2002; p 77.
(7) Bentien, A.; Paschen, S.; Pacheco, V.; Grin, Y. N.; Steglich, F. *Proceedings of the 22nd International Conference on Thermoelectrics ICT2003*, La Grand Motte, France, August, 2003; IEEE: Piscataway, NJ, 2003; p 131.
(8) Demkov, A. A.; Sankey, O. F.; Schmidt, K. E.; Adams, G. B.; O'Keeffe, M. *Phys. Rev. B* **1994**, *50*, 17001.
(9) Llanos, J. Ph.D. Thesis, Universität Stuttgart, 1983.
(10) Zhao, J. T.; Corbett, J. D. *Inorg. Chem.* **1994**, *33*, 5721.
(11) von Schnering, H. G.; Kroner, R.; Baitinger, M.; Peters, K.; Nesper, R.; Grin, Y. *Z. Kristallogr. - New Cryst. Struct.* **2000**, *215*, 205–206.
(12) Dubois, F.; Fassler, T. F. *J. Am. Chem. Soc.* **2005**, *127*, 3264–3265.
(13) Carrillo-Cabrera, W.; Curda, J.; Peters, K.; Paschen, S.; Baenitz, M.; Grin, Y.; von Schnering, H. G. *Z. Kristallogr. - New Cryst. Struct.* **2000**, *215*, 321.
(14) Carrillo-Cabrera, W.; Budnyk, S.; Prots, Y.; Grin, Y. *Z. Anorg. Allg. Chem.* **2004**, *630*, 2267.
(15) Okamoto, N. L.; Tanaka, K.; Inui, K. *Acta Mater.* **2006**, *54*, 173.
(16) Carrillo-Cabrera, W.; Gil, R. C.; Paschen, S.; Grin, Y. *Z. Kristallogr. - New Cryst. Struct.* **2002**, *217*, 183–185.
(17) Okamoto, N. L.; Kishida, K.; Tanaka, K.; Inui, K. *J. Appl. Phys.* **2006**, *100*, 073504.
(18) Iversen, B. B.; Palmquist, A. E. C.; Cox, D. E.; Nolas, G. S.; Stucky, G. D.; Blake, N. P.; Metiu, H. *J. Solid State Chem.* **2000**, *149*, 455.
(19) Chakoumakos, B. C.; Sales, B. C.; Mandrus, D. G.; Nolas, G. S. *J. Alloys Compd.* **2000**, *296*, 80.

10.1021/cm8028559 CCC: $40.75
Published on Web 03/27/2009

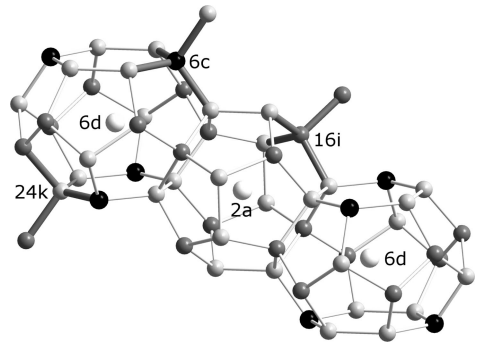

Figure 1. Generic clathrate type I structure of the $A_8M_xX_{46-x-y}\square_y$ compounds (A = group IA or IIA elements, M = group VIII, IB, IIB, or IIIA elements, X = group IV elements, and □ = vacancy). The 20-atom cage is filled by the A-atom (white sphere) at the 2a site while the 24-atom cages are centered on the A atoms at the 6d site. The 6c site (black sphere), 16i site (medium gray sphere), and 24k site (light gray sphere) are marked for better clarity. In the generic structure, the vacancies only occupy the 6c site while the M and X atoms can occupy any of the 6c, 16i, and 24k sites. Specifically, Zn only occupies the 6c site when $x \leq 6$.

typical of crystalline degenerated (narrow band) semiconductors which can be ascribed to the $[Ga_{16}Ge_{30}]$ network. For instance, for single crystalline $Ba_8Ga_{16}Ge_{30}$, at 300 K, $\rho = 0.7$ mΩ·cm, $\alpha = -50\ \mu V \cdot K^{-1}$, and this compound displays a dimensionless figure of merit $ZT = \alpha^2 T/\lambda\rho$[20] larger than unity at 900 K (ZT = 1.4).[5] Band structure calculations for the $A_8Ga_{16}Ge_{30}$ compounds (A = Sr, Ba, Eu) confirmed that they are semiconductors which fulfill the Zintl rule: the eight A^{2+} atoms donate their 16 electrons to the $[Ga_{16}Ge_{30}]$ network, and (4b)Ge^0 and (4b)Ga^{1-} respectively behave like 0-1-electron acceptors.[21,22] Assuming that transition elements also follow the Zintl rule, the M components from respectively groups IIIA, IIB, IB, and VIII may formally behave like 1-2-3-4-electron acceptors. Similarly, in Ge-based clathrates, the vacancies should behave like 4-electron acceptors. This has been experimentally[23] and theoretically[24] verified in the Sn-based type I clathrate $Cs_8Sn_{44}\square_2$ which is a narrow-gap semiconductor. Band structure calculations are required to check that this is effectively the case in $Ba_8Ge_{43}\square_3$.[25] The occurrence of vacancies on the Ge network implies that the charge carrier concentration and electronic transport properties are controlled not only by the M-metal concentration but also by the vacancies concentration.

The $Ba_8Zn_xGe_{46-x-y}\square_y$ compound was first reported by Kuhl et al.[26] who concluded that the phase has a homogeneity range for $4 \leq x \leq 8$ and that these compounds exist and crystallize in the clathrate type I structure. On the basis of their X-ray single crystal data, Kuhl et al. showed that y increases when x decreases and suggested the relation $y = 4 - x/2$ between the vacancies and zinc concentrations which implies Zintl behavior, complete charge compensation, and semiconducting properties for the whole x range. This suggestion seemed promising for the thermoelectric properties of the Zn-substituted clathrates since the highest power factors (α^2/ρ) were found in Ga-based type I clathrates with formally complete charge compensation (x(Ga) = 16).[17] We therefore decided to explore the electronic transport properties of $Ba_8Zn_xGe_{46-x-y}\square_y$ as a function of the compositional parameters x and y. However, as will be seen, since the vacancy concentration and Zn concentration are related in the $Ba_8Zn_xGe_{46-x-y}\square_y$ series, this does not provide two independent parameters to play on the thermoelectric properties. The charge carrier concentration ($[n]$) in the $Ba_8Zn_xGe_{46-x-y}\square_y$ compound is bound between ~ 0 and 4 electrons/formula unit, and we obtained good thermoelectric properties when $x \sim 8$, which corresponds to $[n] \sim 0$. During the course of this work, Melnychenko-Koblyuk et al.[27] and Christensen et al.[28] also reported on the $Ba_8Zn_xGe_{46-x-y}\square_y$ compound. Reference 28 mainly deals with the host (Ge/Zn)−guest (Ba) coupling in $Ba_8Zn_8Ge_{38}$, a question which we do not address here. The broader scope of reference 27 encompasses the structural, thermal, phonon, and transport properties of the $Ba_8Zn_xGe_{46-x-y}\square_y$ ($0 \leq x \leq 8$). The results of their work which are common to ours agree, but they are usually obtained by different techniques. We provide a detailed and thorough characterization of the vacancies as well as an explanation for their stoichiometry.

Experimental Section

The polycrystalline samples $Ba_8Zn_xGe_{46-x-y}\square_y$ (nominal compositions $x = 2-4$, $5-8$, $y = 0-2$) were obtained in a two-step synthesis. Ba (99%) with 3% mass excess and Ge (99.999%) were first arc-melted on a copper hearth under argon. This coarsely crushed Ba−Ge precursor was placed in a vitreous carbon crucible, and the proper amount of Zn (99.9%) was added. The crucible was sealed in a quartz tube under partial Ar atmosphere and heated to 980 °C for 12 h, cooled down to and annealed for 4−6 days at 900 °C, and furnace-cooled to room temperature. Two $x = 8$ samples, labeled A and B, were prepared. Typical weight losses are 3% after the first step, compensated by the Ba excess, and 1% after the second step. Differential thermal analysis performed on $Ba_8Zn_8Ge_{38}$ (B) showed that this phase melts congruently at 941 °C.

X-ray powder diffraction intensities (Cu Kα radiation) were recorded in the 2θ range [10−110°] on a Brüker D8 diffractometer. The patterns were processed with the Rietveld method using the program FULLPROF.[29] The diffraction line profile was chosen to be pseudo-Voigt (Berar and Baldinozzi asymmetry), and the background was fitted by linear interpolation within a set of points. The lattice parameter of the clathrate type I phase as well as the coordinates of the Ge (16i) and the Ge (24k) atoms were the main parameters to be refined. The anisotropic atomic displacement parameters were refined while the site occupancy was held fixed

(20) The efficiency of a thermoelectric device qualitatively varies like the figure of merit ZT of its constituting materials. A ZT larger than unity is considered as a necessary condition for applications.

(21) Blake, N. P.; Bryan, J. D.; Latturner, S.; Mollnitz, L.; Stucky, G. D.; Metiu, H. *J. Chem. Phys.* **2001**, *114*, 10063.
(22) Madsen, G. K. H.; Schwarz, K.; Blaha, P.; Singh, D. J. *Phys. Rev. B* **2003**, *68*, 125212.
(23) Nolas, G. S.; Cohn, J. L.; Nelson, E. *Proceedings of the 18th International Conference on Thermoelectrics*, Baltimore, MD, U.S.A., Aug 29−Sept 2, 1999; IEEE: Piscataway, NJ, 1999; p 493.
(24) Myles, C. W.; Dong, J.; Sankey, O. F. *Phys. Rev. B* **2001**, *64*, 165202.
(25) Okamoto, N. L.; Oh, M. W.; Nishii, T.; Tanaka, K.; Inui, K. *J. Appl. Phys.* **2006**, *99*, 033513.
(26) Kuhl, B.; Czybulka, A.; Schuster, H. U. *Z. Anorg. Allg. Chem.* **1995**, *621*, 1.
(27) Melnychenko-Koblyuk, N.; Fornasini, L.; Kaldarar, H.; Michor, H.; Röhrbacher, F.; Koza, M.; Royanian, E.; Bauer, E.; Rogl, P.; Rotter, M.; Schmid, H.; Marabelli, F.; Devishvili, A.; Doerr, M.; Giester, G. *J. Phys., Condens. Matter* **2007**, *19*, 216223.
(28) Christensen, M.; Iversen, B. B. *J. Phys.: Condens. Matter* **2008**, *20*, 104244.
(29) Rodriguez-Carvajal, J. *Physica B* **1993**, *192*, 55–69.

Table 1. Phases and Their Composition of the $Ba_8Zn_xGe_{46-x-y}\square_y$ Samples[a]

nominal composition	measured composition of the clathrate I phase	secondary phase
$Ba_8Zn_8Ge_{38}$ (A)	$Ba_{7.95(3)}Zn_{7.83(6)}Ge_{38.17(6)}$	$BaZn_2Ge_2$ (3%)
$Ba_8Zn_8Ge_{38}$ (B)	$Ba_{7.93(3)}Zn_{7.53(3)}Ge_{38.47(4)}$	$BaZn_2Ge_2$ (4%)
$Ba_8Zn_7Ge_{39}$	$Ba_{7.95(3)}Zn_{7.1(1)}Ge_{38.9(1)}$	Ge (1%)
$Ba_8Zn_6Ge_{39}\square_1$	$Ba_{8.00(2)}Zn_{6.3(1)}Ge_{39.7(1)}$	
$Ba_8Zn_4Ge_{42}$	$Ba_{8.00(3)}Zn_{4.14(8)}Ge_{40.73(8)}$	$Ba_6(Ge/Zn)_{25}$ (2%)
$Ba_8Zn_3Ge_{40.5}\square_{2.5}$	$Ba_{8.00(5)}Zn_{3.96(6)}Ge_{41.00(8)}$	$Ba_6(Ge/Zn)_{25}$ (10%)
$Ba_8Zn_2Ge_{41}\square_2$	$Ba_{8.0(2)}Zn_{2.3(2)}Ge_{41.5(1)}$	$Ba_6(Ge/Zn)_{25}$ (44%), Ge (4%)

[a] The EPMA measured compositions for $x \leq 6$ were obtained by normalizing at [Ba] = 8 while those for $x \geq 6$ were obtained by normalizing at x + [Ge] = 46 (see text for explanation). The estimated standard deviations of the compositions are given in parentheses.

to the value measured by electron probe micro-analysis (EPMA) because of the strong correlation between these parameters. The secondary phases were included in these Rietveld refinements, and an estimate of their mass fraction could also be obtained.

EPMA of the barium, zinc, and germanium fractions was performed with a CAMECA SX100 electron microprobe ($V = 15$ kV, $I = 60$ nA) using $BaSO_4$, ZnSe, and Ge as standards. Average concentration and standard deviation of the matrix concentrations was obtained from a set of 70 individual measurements spread over a region of ~100 μm × 100 μm. The atomic fractions (Table 1) were obtained by considering that the Ba site is fully occupied for $x \leq 6$ (normalized at 8 Ba atoms per formula unit (f.u.)) and that no Zn or Ge vacancies exist for $x \geq 6$ (normalized at 46 Zn + Ge atoms/f.u.). EPMA of the Ba_8Ge_{43} phase (see Figure 5) was performed on a multiphase sample with nominal composition Ba_6Ge_{25}.

The high-resolution transmission electron microscopy (HR-TEM) experiments were carried out at the TEM Laboratory Triebenberg for Electron Holography and High-Resolution Microscopy of the TU Dresden, Germany. A field emission microscope CM 200 FEG/ST-Lorentz (FEI, Eindhoven) at an acceleration voltage of 200 kV equipped with a Gatan 1 × 1 k slow-scan camera was used. The point resolution amounts to 2.4 Å and the information limit to about 2.0 Å. The analyses of the TEM images were realized by means of the Digital Micrograph software (Gatan, U.S.A.). The selected area electron diffraction (SAED) patterns were obtained with a FEI Tecnai 10 (LaB_6 source and 100 kV acceleration voltage) equipped with a CCD camera (model Temcam-F224HD from TVIPS, Garching, Germany).

Samples for electronic transport measurements were cut from the buttons with a diamond saw. Seebeck coefficient measurements were carried out on 8 × 1.5 × 1.5 mm^3 bar-shaped specimens at room temperature with a constant thermal gradient $\Delta T = 1$ K using a homemade apparatus with Chromel/Constantan thermocouples.[30] Electrical resistivity and Hall effect measurements were performed on square shape samples (~4 × ~4 × ~0.4 mm^3) between 5 and 300 K using the Van der Pauw method in a Quantum Design PPMS in ac-mode ($\nu = 107$ Hz).[31] The Hall coefficient R_H was deduced from the relation $R_H = t \times \Delta R/\Delta H$ with the sample thickness t and $\Delta R/\Delta H$ the slope of the Hall resistance versus field curve between −5 and 5 T. The charge carrier concentration [n] was calculated from the Hall coefficient R_H, assuming a single-carrier model and a Hall factor of unity.

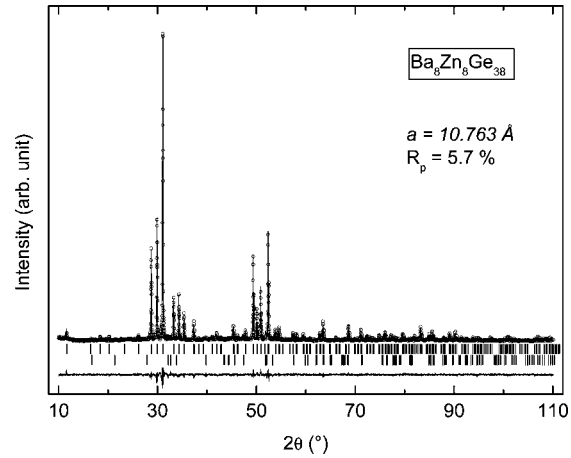

Figure 2. Experimental (circle) and calculated (line) diffraction patterns of the $Ba_8Zn_8Ge_{38}$ sample (A). The vertical lines in the middle correspond to the Bragg positions of the two contributions to the pattern ($Ba_8Zn_8Ge_{38}$ with the type I clathrate structure and $BaZn_2Ge_2$ with the $ThCr_2Si_2$ structure type). The bottom line is the difference between experience and calculation.

Crystal Structure and Elemental Composition

The diffraction patterns of the $Ba_8Zn_xGe_{46-x-y}\square_y$ samples ($2 \leq x \leq 8$) were successfully interpreted assuming a type I clathrate structure for the $Ba_8Zn_xGe_{46-x-y}\square_y$ phase. For instance, Figure 2 shows the Rietveld refinement results for $Ba_8Zn_8Ge_{38}$ (sample A): a good reliability factor ($R_p = 5.7\%$) and a lattice parameter ($a = 10.763(1)$ Å) close to the values previously reported[26,27] are obtained. In a preliminary account of this work,[32] we reported the observation of extra faint satellite lines in every diffraction pattern of the $Ba_8Zn_xGe_{46-x-y}\square_y$ samples ($4 \leq x \leq 8$) which could not be indexed within the clathrate type I structure and were initially indexed within a $4a \times 4a \times 4a$ supercell. This triggered a direct observation of the reciprocal lattice of these compounds by electron diffraction (SAED images) and by fast Fourier transform (FFT) of the HRTEM images. In the reciprocal space images shown in Figure 3 and in the inset of Figure 4, every observed diffraction spot of the [100], [110], [112], [115], and [122] zones could be indexed with a cubic primitive lattice and $a = 10.763$ Å. Hence, no superstructure could be observed by SAED or HRTEM. The apparent contradiction between the structure deduced from the first XRD and that obtained by (HR)TEM was resolved by changing the X-ray tube of the X-ray diffractometer used in this study.[32] It can therefore be concluded that the $Ba_8Zn_xGe_{46-x-y}\square_y$ compounds ($4 \leq x \leq 8$) crystallize with the type I clathrate structure. Since $Ba_8Ga_3Ge_{43-y}\square_y$ has been reported[17] to crystallize within the $Ba_8Ge_{43}\square_3$ structure type which is a superstructure of the clathrate type I structure ($a = 2a_I$ and space group $Ia\bar{3}d$), we examined this possibility for the $x = 2$ sample. No superstructure line could be unambiguously detected in the pattern of the $x = 2$ sample: several lines belonging to the impurity phase $Ba_6(Zn/Ge)_{25}$ were overlapping with the possible 2θ positions of superstructure lines. Even if we cannot completely exclude the

(30) Bérardan, D.; Alleno, E.; Godart, C.; Rouleau, O.; Rodriguez-Carvajal, J. *Mater. Res. Bull.* **2005**, *40*, 537–551.
(31) Performing van der Pauw measurements. http://www.qdusa.com/resources/pdf/ppmsappnotes/1076-304.pdf, Quantum Design, San Diego, 2007.
(32) Alleno, E.; Maillet, G.; Rouleau, O.; Leroy, E.; Godart, C. *Proceedings of the 5th European Conference on Thermoelectrics*, Odessa, Ukrain, 2007; Thermion: Odessa, 2007; p 108.

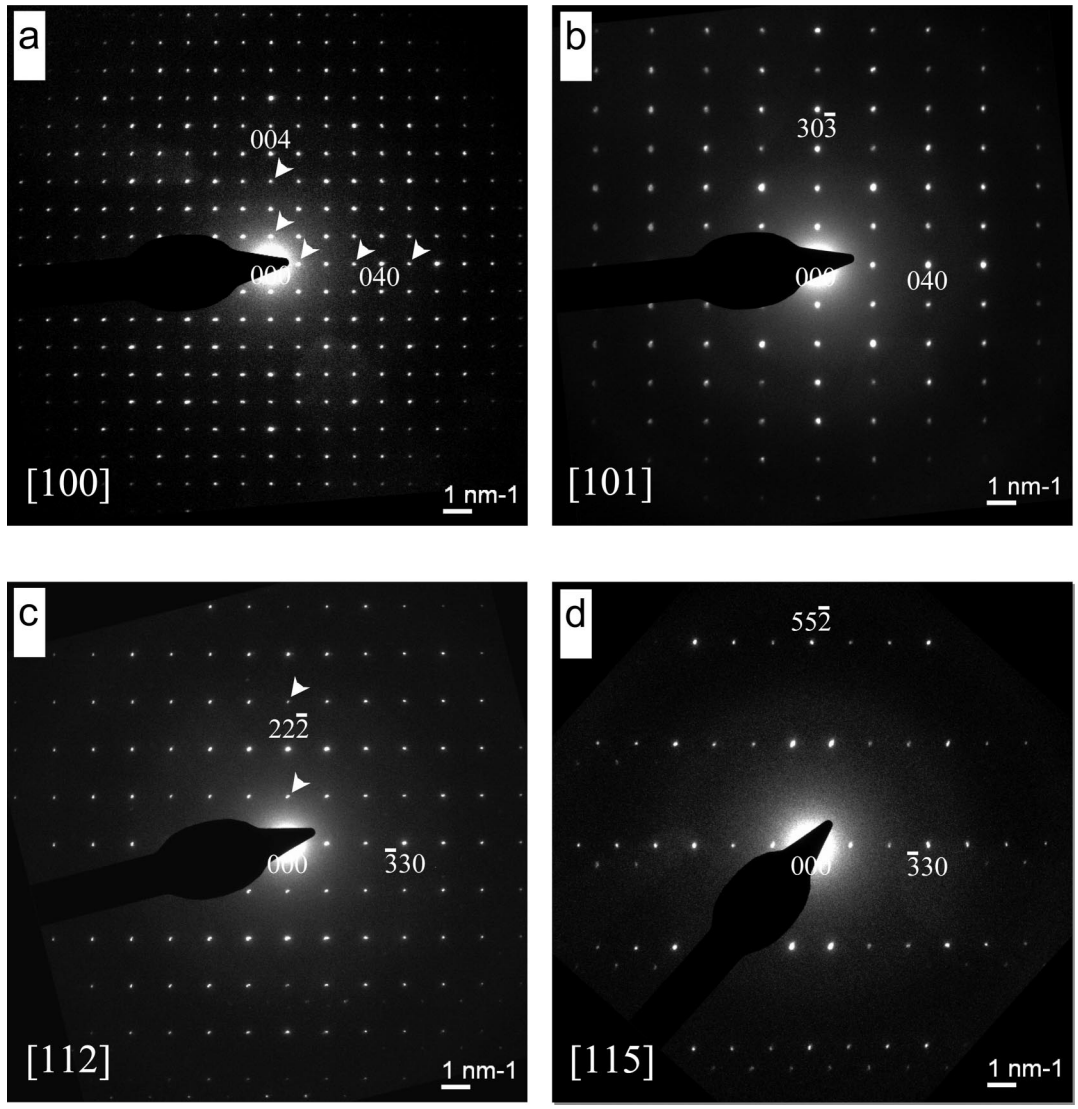

Figure 3. Selected area electron diffraction (SAED) pattern of $Ba_8Zn_8Ge_{38}$ (sample A). Panels a, b, c, and d display the [100], [101], [112], and [115] zones in reciprocal space, respectively. No superlattice reflections are observed. Forbidden reflections (marked by arrows) appear in [100] and [112] zones due to dynamical effects.

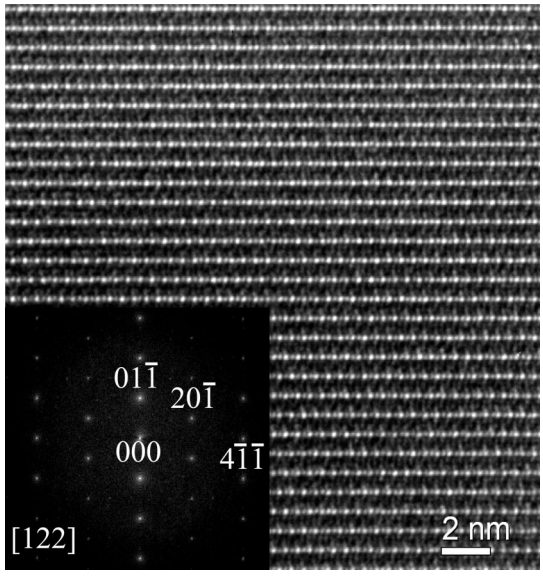

Figure 4. HRTEM image of $Ba_8Zn_8Ge_{38}$ (sample A) along the [122] direction. The fast Fourier transformation (FFT) pattern, included as inset, does not show superlattice reflections.

possibility for the $x = 2$ sample to crystallize with the $Ba_8Ge_{43}\square_3$-like superstructure, we could satisfactorily refine the $x = 2$ pattern with the clathrate type I structure, in agreement with ref 27.

Backscattered electron images of samples with nominal composition $x = 2, 4, 6, 8$ (sample B) obtained with the electron microprobe are shown in Figure 5. The elemental composition measurements confirmed that the $x = 4-8$ samples contain the $Ba_8Zn_xGe_{46-x-y}\square_y$ clathrate as the majority phase (medium gray) with the measured zinc concentration very close to its nominal value. The $x = 6$ sample is single phase. Only few inclusions of $BaZn_2Ge_2$ (light gray) in the $x = 8$ sample and $Ba_6(Zn/Ge)_{25}$ (light gray) in the $x = 4$ sample could be detected as secondary phases. $BaZn_2Ge_2$ has been reported to crystallize within the $ThCr_2Si_2$ structure ($a = 4.527$ Å, $c = 10.555$ Å)[33] and $Ba_6(Zn/Ge)_{25}$ is a solid solution of Zn in Ba_6Ge_{25},[34] a type IX clathrate

(33) Proserpio, D. M.; Artioli, G.; Mulley, S.; Chacon, G.; Zheng, C. *Chem. Mater.* **1997**, *9*, 1463.
(34) Carrillo-Cabrera, W.; Curda, J.; von Schnering, H. G.; Paschen, S.; Grin, Y. N. *Z. Kristallogr.* **2000**, *215*, 207.

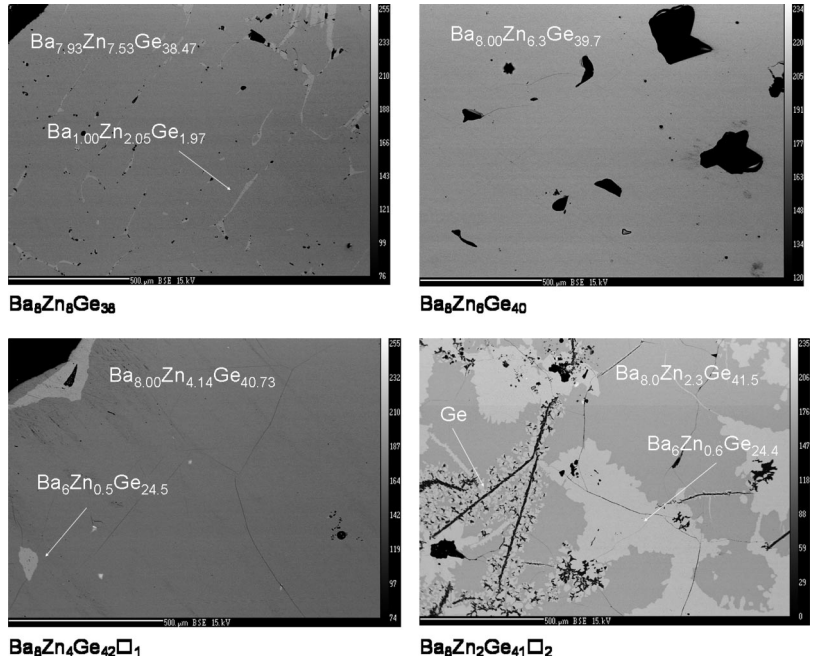

Figure 5. Back-scattering electron images obtained with the electron microprobe for the $x = 2$, 4, 6, and 8 (B) samples. The black regions are holes.

Table 2. Crystallographic Data of $Ba_8Zn_xGe_{46-x-y}\square_y$: Lattice Parameters, Unit Cell Volumes, Atomic Coordinates (x, x, x) for E(16i) and (0, y, z) for E(24k), and Reliability Factors

composition	a (Å)	V (Å^3)	x (16i)	y, z (24k)	R_p (%)
$Ba_{7.95}Zn_{7.83}Ge_{38.17}$ (A)	10.763	1246.81	0.184(1)	0.311(2), 0.117(2)	5.7
$Ba_{7.93}Zn_{7.53}Ge_{38.47}$ (B)	10.762	1246.46	0.185(1)	0.312(2), 0.115(2)	6.9
$Ba_{7.95}Zn_{7.1}Ge_{38.9}$	10.756	1244.38	0.184(1)	0.310(2), 0.117(2)	6.0
$Ba_8Zn_{6.29}Ge_{39.69}$	10.747	1241.26	0.184(1)	0.312(1), 0.119(1)	4.7
$Ba_8Zn_5Ge_{40.5}\square_{0.5}$[a]	10.736	1237.45	0.184(1)	0.312(3), 0.119(3)	5.8
$Ba_8Zn_{4.14}Ge_{40.73}\square_{1.13}$	10.715	1230.20	0.183(1)	0.314(1), 0.120(1)	6.7
$Ba_8Zn_{3.96}Ge_{41}\square_{1.04}$	10.710	1228.48	0.182(2)	0.317(2), 0.120(3)	6.2
$Ba_8Zn_{2.34}Ge_{41.54}\square_{1.92}$	10.688	1220.93	0.183(2)	0.319(3), 0.121(4)	6.9

[a] The composition of the $x = 5$ sample was taken as nominal.

with Ge partially substituted by Zn. The $x = 2$ sample displays a multiphase microstructure with $Ba_8Zn_{2.3}Ge_{41.5}$ and $Ba_6(Zn/Ge)_{25}$ as the main phases (measured composition) and large inclusions of Ge at the grain boundaries. Despite this equilibrium situation between these three phases in the x= 2 sample, the measured composition $Ba_8Zn_{2.34}Ge_{41.54}$ shows that the composition "$Ba_8Zn_2Ge_{42}\square_2$" belongs to the clathrate phase and the effective zinc composition is very close to the nominal one. Moreover, this composition which had not been reported by Kuhl et al.[26] has been obtained as a single phase sample in ref 27 with different synthesis conditions. This elemental microanalysis is consistent with the X-ray analysis which gave the same phase identification and yielded the mass percentage of each phase. The results of the chemical analysis of the phases occurring in the $Ba_8Zn_xGe_{46-x-y}\square_y$ samples are summarized in Table 1. It is noticeable that the measured zinc concentration is smaller than the measured barium concentration in the two $Ba_8Zn_8Ge_{38}$ samples: this will explain the observed n-type behavior of the electron transport properties. The results of the refinements of the crystal structure are summarized in Table 2.

Zn Site Selectivity and Ge Vacancies

A plot of the vacancies concentration (y), deduced from the relation $y = 46 - (x + [Ge])$, with x and [Ge] respectively the measured Zn and Ge content per formula unit, as a function of x is displayed in Figure 6 (left vertical axis). It first shows that in the $Ba_8Zn_xGe_{46-x-y}\square_y$ series, the vacancies concentration is dependent on the zinc content. This had also been previously noticed in $Ba_8Ga_xGe_{46-x}\square_y$,[17] in $Ba_8Cd_xGe_{46-x-y}\square_y$,[35] and in $Ba_8Zn_xGe_{46-x-y}\square_y$.[26,27] The vacancies concentration y decreases linearly upon Zn substitution from ~3.3 for $x = 0$ to $y = 0$ for $x = 6$. The value $y = 3.3$ measured in our multiphase $Ba_6Ge_{25}-Ba_8Ge_{43}\square_3$ sample by EPMA is consistent with the $Ba_8Ge_{42.9}\square_{3.1}$ composition reported in ref 14. A best fit of the data gives $y = 3.3 - 0.54x$ for $0 \le x \le 6$. Since the vacancies have been shown to occur on the 6c site[36] in $Ba_8Ge_{42.7}\square_{3.3}$,[14,15] the fact that y reaches 0 at $x = 6$ demonstrates that zinc atoms both fill the vacancies and replace Ge atoms in the 6c position of the clathrate type I structure. Authors in refs 26 and 27 had also concluded that Zn substitutes the 6c site in $Ba_8Zn_xGe_{46-x-y}\square_y$. However, in the former reference, the proposed relations $y = 4 - x/2$ between the vacancy and

(35) Melnychenko-Koblyuk, N.; Grytsiv, A.; Berger, S.; Kaldarar, H.; Michor, H.; Röhrbacher, F.; Royanian, E.; Bauer, E.; Rogl, P.; Schmid, H.; Giester, G. *J. Phys., Condens. Matter* **2007**, *19*, 046203.

(36) The 6c site in the type I structure corresponds to the 24c site in the 2a superstructure which actually describes Ba_8Ge_{43}.

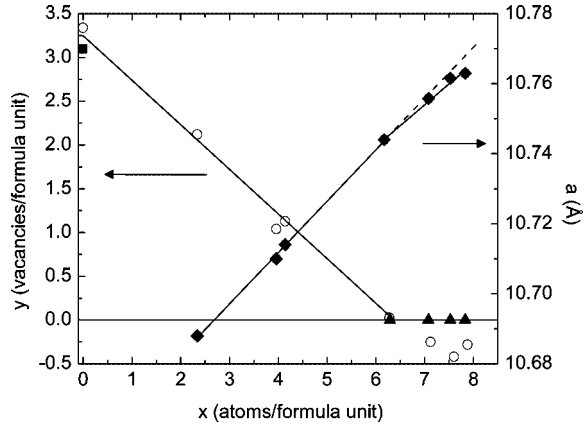

Figure 6. Left axis: number of vacancies (y) in $Ba_8Zn_xGe_{46-x-y}\square_y$ as a function of the measured Zn fraction (x). The open circles correspond to the [Ba] = 8 normalization of the atomic fraction while the filled triangles correspond to the x + [Ge] = 46 normalization. The filled square is the vacancies fraction in $Ba_8Ge_{43}\square_3$ reported in ref 14. The solid line is a linear best fit ($y = 3.3 - 0.54x$) to the experimental data (open circle) for $0 \le x \le 6$. Right axis: lattice parameter (filled diamond) of the type I structure in $Ba_8Zn_x\ Ge_{46-x-y}\square_y$ as a function of the measured (EPMA) Zn concentration x. The two solid lines are linear fits to the data for $x \le 6$ and $x \ge 6$.

the zinc concentrations is not consistent with our experimental data, while in the latter reference, no explicit relation between y and x is proposed. A careful structural study on $Ba_8M_{16}Ge_{30}$ (M = Al, In, Ga)[37] and phase stability calculations[21] showed that the group IIIA elements preferentially occupy the 6c sites, and this seems to be a general feature of the type I clathrates.

The relation $y = 3.3 - 0.54x$ reveals a complex mechanism of the zinc implementation into the crystal structure of $Ba_8Ge_{43}\square_3$. The coefficient 0.54 corresponds to the fact that when two Zn atoms are inserted in the crystal structure of $Ba_8Ge_{43}\square_3$, only approximately one Zn atom fills a vacancy while another Zn atom replaces a Ge atom. This complex implementation of Zn in the clathrate network can be understood from a simplified band picture related to the formation of vacancy. This formation results from a balance between the energy loss of reducing the number of occupied bonding states (valence band) and the energy gain of transferring electron from antibonding states (conduction band) to nonbonding states energetically located in between.[24,38] Assuming the formal oxidation numbers 0 for (4b)Ge, 2− for (4b)Zn, and 4− for a vacancy, filling a vacancy by a zinc atom transforms eight filled nonbonding states into eight filled bonding states (energy gain) and adds two electrons to antibonding states (energy loss). This addition of two electrons to antibonding states (energy loss) can be compensated by replacing a Ge atom by another Zn atom which removes these two electrons from antibonding states (energy gain), and the total number of electrons of $Ba_8Ge_{43}\square_3$ is recovered. Filling only vacancies would transform more filled nonbonding states into filled bonding state, but the number of electrons in the nonbonding states would increase. Conversely, substituting only Ge atoms would reduce the number of electrons in the antibonding states but keep unchanged the number of filled nonbonding states. In $Ba_8Zn_xGe_{46-x-y}\square_y$, the filling of approximately one vacancy accompanied by the substitution of a Ge atom is thus the only scenario which maintains the subtle energy balance found in $Ba_8Ge_{43}\square_3$. This leads to a slope for the $y = f(x)$ relation equal to the ratio of the formal oxidation number of (4b)Zn (2−) by the formal oxidation number of a vacancy (4−), that is, (2−)/(4−) = 0.5, close to the experimental value (0.54). Extending this scenario to other $Ba_8M_xGe_{46-x-y}\square_y$ type I clathrates, slopes of the relation $y = f([M])$ respectively equal to 1/4, 1/2, 3/4, and 1 are anticipated when the M component runs across the group IIIA, IIB, IB, and VIII elements. Literature indeed supports this scenario: from the data published by Okamoto for $Ba_8Ga_xGe_{46-x-y}\square_y$,[17] a slope close to 1/4 can be deduced (0.22), and a slope close to 1 (0.8) was reported for $Ba_8Pd_xGe_{46-x-y}\square_y$.[39] This correspondence between the slopes of the $y = f([M])$ relations and the ratio of the metal M oxidation number over the formal oxidation number of a vacancy (4−) seems to be a general feature of the $Ba_8M_xGe_{46-x-y}\square_y$ type I clathrates.

It is expected that for zinc concentration larger than 6, the exceeding zinc atoms substitute on another Ge site(s) and the vacancies concentration remains equal to zero. This requires a change of the normalization scheme to convert the atomic fractions into formula unit. Up to now, we assumed [Ba] = 8. For $x < 6$ it should be replaced by x + [Ge] = 46, consistent with the fact that the 6c site is fully occupied for $x = 6$. This change of normalization across the data of Figure 6 is legitimated by the cross-over at $x = 6$, where both normalizations yield the same elemental composition. This new choice of normalization scheme leads to the effective composition $Ba_{7.93}Zn_{7.53}Ge_{38.47}$ for $Ba_8Zn_8Ge_{38}$ sample B and suggests that vacancies ($\sim$ 0.05/unit cell, see Table 1) occur on the barium sites for $x > 6$.

In Figure 6 (right vertical axis), the lattice parameter a increases with the zinc content, but the variation is not well described by a simple linear fit. A better agreement is obtained by fitting the experimental data with two different straight lines with slopes 1.47×10^{-2} Å/atom for $x \le 6$ and 1.19×10^{-2} Å/atom for $x \ge 6$. Despite its smallness, the difference between the two lines exceeds our experimental accuracy ($\pm 10^{-3}$ Å), and this indicates that the effect is not an artifact. Here again, at $x = 6$ a cross-over appears which reflects the site selectivity of Zn for the 6c site, and this behavior of the lattice parameter is fully consistent with the EPMA results. Since zinc and germanium have approximately equal radii, the increase of a with x for $x \le 6$ arises rather from another reason than a simple steric argument. Obviously, the filling of the vacancies which require less volume than Zn atoms is this reason. For $6 < x \le 8$, this effect disappears, and anticipating the Hall effect results, Zn substitution in $Ba_8Zn_xGe_{46-x}$ reduces the number of antibonding states and subsequently their contribution to the volume of the framework. The combination of the filled

(37) Bentien, A.; Nishibori, E.; Paschen, S.; Iversen, B. B. *Phys. Rev. B* **2005**, *71*, 144107.
(38) Ramachandran, G. K.; MacMillan, P. F.; Dong, J.; Sankey, O. F. *J. Solid State Chem.* **2000**, *154*, 626.
(39) Melnychenko-Koblyuk, N.; Grytsiv, A.; Rogl, P.; Rotter, M.; Bauer, E.; Durand, G.; Kaldarar, H.; Lackner, R.; Michor, H.; Royanian, E.; Koza, M.; Giester, G. *Phys. Rev. B* **2007**, *76*, 144118.

Table 3. Selected Interatomic Distances (in Å) in $Ba_8Zn_xGe_{46-x-y}\square_y$

	$Ba_{7.93}Zn_{7.53}Ge_{38.47}$	$Ba_{7.95}Zn_{7.1}Ge_{38.9}$	$Ba_8Zn_{6.29}Ge_{39.69}$	$Ba_8Zn_{4.14}Ge_{40.73}$
Ba2a−E16i	3.443(2)	3.433(1)	3.418(1)	3.395(1)
Ba2a−E24k	3.575(2)	3.566(2)	3.591(2)	3.605(2)
Ba6d−E6c	3.805(0)	3.803(0)	3.800(0)	3.788(0)
Ba6d−E16i	3.995(2)	3.995(1)	3.995(1)	3.987(2)
Ba6d−E24k	4.194(2)	4.172(2)	4.153(2)	4.129(2)
E6c−E24k	2.494(2)	2.493(2)	2.461(1)	2.428(2)
E16i−E16i	2.434(2)	2.449(2)	2.470(2)	2.489(2)
E16i−E24k	2.526(2)	2.508(2)	2.510(2)	2.506(2)
E24k−E24k	2.475(3)	2.514(3)	2.548(2)	2.571(3)

Table 4. Selected Angles (in deg) in $Ba_8Zn_xGe_{46-x-y}\square_y$

	$Ba_{7.93}Zn_{7.53}Ge_{38.47}$	$Ba_{7.95}Zn_{7.1}Ge_{38.9}$	$Ba_8Zn_{6.29}Ge_{39.69}$	$Ba_8Zn_{4.14}Ge_{40.73}$
24k−6c−24k	108.8(1)	109.9(1)	109.9(1)	110.0(1)
24k−6c−24k	109.8(1)	109.3(1)	109.2(1)	109.2(1)
16i−16i−24k	108.3(1)	108.1(1)	107.2(1)	106.4(1)
24k−16i−24k	110.6(1)	110.8(1)	111.6(1)	112.4(1)
6c−24k−16i	105.5(1)	106.0(1)	107.0(1)	107.8(1)
6c−24k−24k	125.6(1)	125.1(1)	125.0(1)	125.0(1)
16i−24k−16i	103.8(1)	104.4(1)	103.7(1)	102.9(1)
16i−24k−24k	107.3(1)	106.8(1)	106.2(1)	105.6(1)

vacancies with the reduction the number of antibonding states thus leads to the smaller gradient da/dx.

Table 3 reports selected atomic distances in $Ba_8Zn_xGe_{46-x-y}\square_y$ ($x = 4.14, 6.29, 7.1, 7.53$). The Ba−$E$ (E = Zn or Ge) distances weakly vary upon Zn substitution: the Ba(6d)−E(6c) and Ba(6d)−E(16i) distances are nearly constant while the Ba(2a)−E(16i), Ba(2a)−E(24k), and Ba(6d)−E(24k) exhibit less than 2% variation when x varies from 4 to 8. This implies a good stability of the size of the cages, and one can also speculate a weak change of the lattice thermal conductivity upon Zn substitution. The distances in the Zn/Ge framework display significantly stronger variations than the sizes of the cages, directly reflecting the evolution of the chemical formula. Nonetheless, the values and the variations of the distances with x do not allow a clear distinction of the 6c sites from the 16i and 24k site and do not help us understand how this site is preferentially occupied by M-substituting atoms and Ge vacancies. For better clarity of the next discussion, Figure 1 shows a representation of the clathrate type I structure where the 6c, 16i, and 24k sites have been marked. Examination of the values of the 3-site angles displayed in Table 4 reveals a more distinctive feature for the 6c site since the (24k−6c−24k) angle is the closest to the angle of the regular tetrahedron (109.5°): the 3-site angles around the 16i site are close to 108° and 110° respectively while the three bond angles around the 24k site are close to 104°, 106°, and 125°. The environment of the 6c site is less distorted while the 24k site has the most distorted coordination. Empirical potential calculations on various clathrate structures showed that the cohesive energy decreases with the increase of the bond angle deviation from the regular tetrahedron.[40] These results suggest that the site energy (ε) of the three tetrahedrally bonded sites is ordered like $\varepsilon(6c) < \varepsilon(16i) < \varepsilon(24k)$. This would also explain why the substituted metals and vacancies preferentially occupy the 6c site. For $x > 6$, neutron studies reported inconsistent

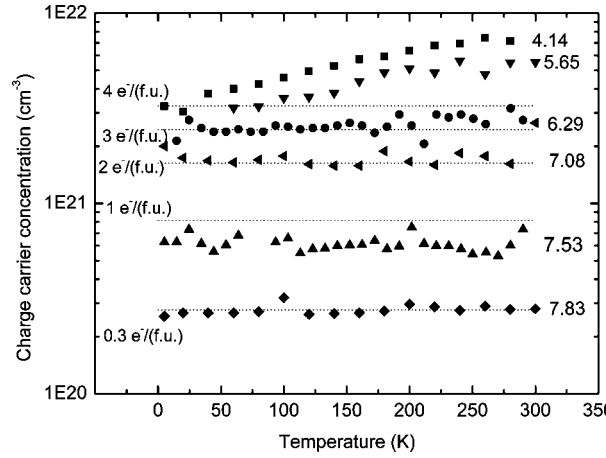

Figure 7. Thermal variations of the charge carrier number ([n]) derived from Hall effect measurements in $Ba_8Zn_xGe_{46-x-y}\square_y$. For comparison, integer electron densities are plotted as dashed lines and reported on the left side of the figure in electron per formula unit. The measured zinc fractions are reported on the right side.

results on the Zn site occupancy. On the one hand, Christensen et al.[28] reported that, in their "slow cooled" $Ba_8Zn_8Ge_{38}$ sample, Zn is equally distributed over both the 16i and the 24k sites while in their "fast cooled" $Ba_8Zn_8Ge_{38}$ sample Zn is nearly completely sitting in the 24k site. On the other hand, Zn was found to preferentially occupy the 16i site over the 24k site by Melnychenko-Koblyuk et al. in $Ba_8Zn_8Ge_{38}$[27] and by Qiu et al. in $Sr_8Zn_8Ge_{38}$.[41] Taking these contradictory results as they are, one can speculate that despite a smaller distortion of the 16i site compared to the 24k site, both sites display similar contribution to the lattice energy.

Charge Carrier Concentration and Transport Properties

Hall effect measurements were carried out on $Ba_8Zn_xGe_{46-x-y}\square_y$ with $4 < x < 8$ (the nearly single phase samples). In every sample, the measured Hall coefficients were negative implying that electrons are the majority charge carriers. Even the two $Ba_8Zn_8Ge_{38}$ samples are n-type conductors, consistent with the observed x understoichiometry ($x < 8$, see Table 2). The concentration of charge carriers ([n]) plotted in Figure 7 is weakly dependent on temperature over the temperature interval [5−300 K], and it ranges from 2.5×10^{20} to 3.3×10^{21} electron/cm^3. This is typical of "bad metals" or of semiconductors with a very large density of charge carriers, that is, a degenerate semiconductor.[42]

To compare with values derived from the Zintl rule, the low temperature number of carriers [n_0] (e$^-$/(f.u.)) measured in $Ba_8Zn_xGe_{46-x-y}\square_y$ is plotted in Figure 8 as a function of the measured zinc concentration x.[43] $Ba_8Ge_{42.7}\square_{3.3}$ is reported as a semiconductor in literature,[25,44] and this corresponding

(40) Moriguchi, K.; Munetoh, S.; Shintani, A.; Motooka, T. *Phys. Rev. B* **2001**, *64*, 195409.
(41) Qiu, L.; Swainson, I. P.; Nolas, G. S.; White, M. A. *Phys. Rev. B* **2004**, *70*, 035208.
(42) Ibach, H.; Lüth, H. *Solid State Physics*, 2nd ed.; Springer: Berlin, 1995.
(43) The [Zn] = 5.5 for the $x = 5$ sample was deduced from the $a = f$([Zn]) curve displayed in Figure 7 and its lattice parameter value $a = 10.736$ Å.
(44) Herrmann, R. F. W.; Tanikagi, K.; Kawaguchi, T.; Sanadori, K.; Zhou, O. *Phys. Rev. B* **1999**, *60*, 13245.

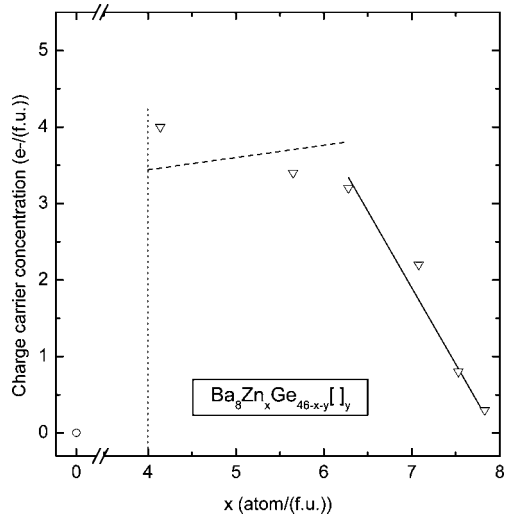

Figure 8. Experimental (triangles), published in ref 25(circles), and calculated (solid line) low temperature electron density ($[n_0]$) as a function of the measured Zn concentration x. The dashed line corresponds to a hypothetical electron concentration calculated from the Zintl rule $[n_0] = 16 - 4y - 2x$ where the number of vacancies $y = 3.3 - 0.54x$ is derived from the EPMA measurements. For $x > 6$, the solid line corresponds to $[n_0] = 2([\mathrm{Ba}] - x)$ with [Ba] and x derived from EPMA.

datum ($[n_0] \sim 0$) is also added in the plot of Figure 8. For $4 \leq x \leq 6$, $[n_0]$ is not ~0 and ranges from 4.0 to 3.2 e^-/formula unit. This last observation is in contradiction with the semiconducting nature of $Ba_8Ge_{42.7}\square_{3.3}$ and with the two Zn^{2-} atoms for one vacancy ($\square^{4-}$) scenario which implies that the number of electrons in the antibonding states (conduction band) should not change and remain nearly equal to 0 e^-/(f.u.) when x increases from 0 to 6. Assuming a formal oxidation number of 4− for a vacancy, a 1.65+ oxidation number is obtained for Ba in semiconducting $Ba_8Ge_{42.7}\square_{3.3}$. This formal oxidation number of Ba smaller than 2+ leaves the possibility for it to increase when Zn is introduced in $Ba_8Ge_{42.7}\square_{3.3}$. The increased number of electrons donated by Ba (from 1.65 to 2 per Ba atom) fill the antibonding states (conduction band) and are responsible for the metallic behavior found in our samples when $4 \leq x \leq 6$. How does this transformation of the electronic state occur in $Ba_8Zn_xGe_{46-x-y}\square_y$ when x increases from 0 to 4: continuously or with a cross-over? Do additional effects such as the reduction of the formal oxidation number of vacancies when $x \leq 6$ is introduced in the crystal structure of $Ba_8Ge_{42.7}\square_{3.3}$ occur? Precise Hall effect measurements and X-ray absorption spectroscopy at the Ba and Ge edges on single-phase samples would be required to answer these questions.

The contradiction between the scenario explaining the implementation of Zn in the $Ba_8Ge_{42.7}\square_{3.3}$ network and the bad metal character of $Ba_8Zn_{4.14}Ge_{40.73}$, for instance, can therefore be lifted by the fact that $Ba_8Ge_{42.7}\square_{3.3}$ has significantly less than four vacancies. The germanium network of $Ba_8Ge_{42.7}\square_{3.3}$ does not need all the valence electrons of Ba for its stabilization, and this compound deviates from the Zintl rule. Similarly, Si-based type I clathrates like Na_8Si_{46} and K_8Si_{46} are non-Zintl metals with no vacancies[38,45] and with a calculated oxidation number for Na and K smaller than 1+ (0.76+ and 0.71+, respectively).[46] Oppositely, the Sn-based clathrate $Cs_8Sn_{44}\square_2$ has two vacancies and is semiconducting, in agreement with the Zintl rule, and a 1+ oxidation number has been calculated for Cs in this compound.[24] Thus, the situation of the binary Ge-based clathrate $Ba_8Ge_{42.7}\square_{3.3}$ regarding the vacancy formation and the Zintl rule is intermediate between the binary Si-based and Sn-based clathrate.

As previously noticed, for $4 \leq x < 6$, $[n_0]$ weakly decreases from 4.0 to 3.2 e^-/formula unit when x increases. Assuming, in agreement with the Zintl rule, the formal oxidation numbers 0 for (4b)Ge, 2− for (4b)Zn, 4− for a vacancy, and 2+ for Ba leads to the calculated variations $[n_0] = (2 \times [\mathrm{Ba}]) - (4 \times y) - (2 \times x) = 2.8 + 0.16 \times x$ (with $y = 3.3 - 0.54 \times x$). This calculation is plotted as a dashed line in Figure 8. There is an overall agreement between the experimental data and the Zintl calculation: the strongest deviation represents approximately 20%. However, this deviation is effective and means that the $Ba_8Zn_xGe_{46-x-y}\square_y$ also weakly deviates from the Zintl rule in the zinc concentration range $4 \leq x \leq 6$. It is difficult to give a precise mechanism leading to the observed weak decrease of $[n_0]$ with x. Here again, one can only speculate on either a reduction of the donor character of Ba and/or to a reduced acceptor character of the vacancies. Deeper and quantitative understanding on how these compounds deviate from the Zintl rule would of course require ab initio electron density calculation. $[n_0]$ exhibits a faster reduction from 3.2 e^-/f.u. to 0.3 e^-/f.u. when $6 < x \leq 8$. In this concentration range, there is no Ge vacancy, and assuming the formal oxidation numbers 0 for (4b)Ge, 2− for (4b)Zn, and 2+ for Ba in agreement with the Zintl rule, the linear expression $[n_0]_{\mathrm{calcd}} = (2 \times [\mathrm{Ba}]) - (2 \times x)$ can be derived (with [Ba] = 7.95). This calculated electron concentration is also plotted in Figure 8, and it models very well the measured $[n_0]$. Thus, the $Ba_8Zn_xGe_{46-x-y}\square_y$ fulfills the Zintl rule when $6 < x \leq 8$, like the $A_8Ga_{16}Ge_{30}$ compounds (A = Sr, Ba, Eu).[21,22] Their charge carrier concentration is bound (at least when $4 \leq x \leq 8$) to moderate values ($0 \leq [n] \leq 4$ e^-/(f.u.) approximately 3.2×10^{21} e^-/cm^3) which corresponds at most to "bad metals" and not to a fully metallic state with $[n] \sim 10^{22}$ e^-/cm^3. This indicates that the $Ba_8Zn_xGe_{46-x-y}\square_y$ structure is not fully flexible and cannot accommodate any charge carrier amount. This is related to its nearly Zintl character previously discussed. However, we will see that since the best thermoelectric properties are obtained in compounds with the lowest electron concentration ($x \sim 8$), this is not a limitation for optimizing the thermoelectric properties of these compounds.

The temperature variations of the resistivity for samples with $x = 4$, 7, 8(A), and 8(B) samples are shown in Figure 9. For all these samples, resistivity weakly increases with temperature, and its room temperature values range between 0.5 and 1.2 mΩ·cm. The weak variations of resistivity with temperature are typical of "bad metals" ($x \sim 4$) or highly degenerate semiconductors ($x \sim 8$). This behavior

(45) Ramachandran, G. K.; MacMillan, P. F.; Diefenbacher, J.; Gryko, J.; Dong, J.; Sankey, O. F. *Phys. Rev. B* **1999**, *60*, 12294.

(46) Volmer, C.; Sternemann, C.; Tse, J. S.; Buslaps, T.; Hiraoka, N.; Bull, C. L.; Gryko, J.; MacMillan, P. F.; Paulus, M.; Tolan, M. *Phys. Rev. B* **2007**, *76*, 233104.

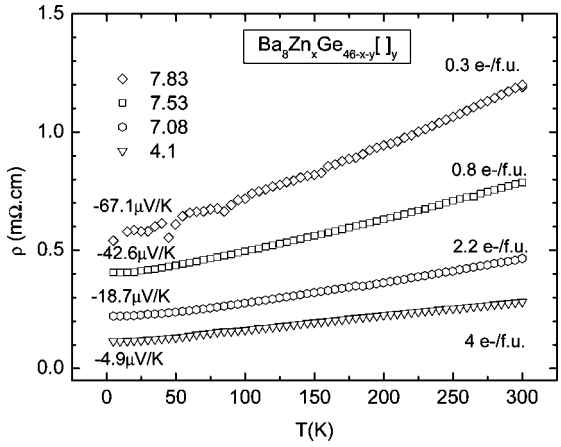

Figure 9. Temperature variation of the resistivity in $Ba_8Zn_xGe_{46-x-y}\square_y$. For each composition, the room temperature values of the Seebeck coefficient and of the measured low temperature electron density ($[n_0]$) are respectively shown on the left and right side of the figure.

has previously been observed for polycrystalline $Ba_8Ga_xGe_{46-x-y}\square_y$.[17] As expected from the variations of the electron density, with increasing zinc concentration, the room temperature resistivity monotonously increases. The absolute value of the room temperature Seebeck coefficient (systematically negative) also increases with x from $-4.9\ \mu V \cdot K^{-1}$ to $-67.1\ \mu V \cdot K^{-1}$ and strictly follows the change of charge carrier concentration. Hence, the sample with the largest power factor is $Ba_{7.95}Zn_{7.83}\ Ge_{38.17}$ (A) with $\alpha^2/\rho = 3.75\ \mu W \cdot K^{-2} \cdot cm^{-1}$ at 300 K. A larger power factor $\alpha^2/\rho = 5.3\ \mu W \cdot K^{-2} \cdot cm^{-1}$ can be calculated from the data reported in ref 27 for their $Ba_8Zn_{7.7}Ge_{38.3}$ sample. Taking the value of ref 28 for the lattice thermal conductivity of $Ba_8Zn_8Ge_{38}$ and adding the electronic contribution using the Wiedemann−Franz law, ZT values of 0.06 and 0.08 are expected at 300 K for our $Ba_{7.95}Zn_{7.83}Ge_{38.17}$ (A) sample and for the $Ba_8Zn_{7.7}Ge_{38.3}$ sample of ref 27, respectively. This range of ZT values compares well with ZT = 0.09 at 300 K published for polycrystalline $Ba_8Ga_{16}Ge_{30}$ by Kuznetsov et al.[47] More transport measurements at high temperature are required to determine the potential of $Ba_8Zn_8Ge_{46}$ for thermoelectric power generation.

Conclusions

When two Zn atoms are implemented in the $Ba_8Zn_xGe_{46-x-y}\square_y$ framework, approximately one fills a vacancy while another substitutes a Ge atom. A simplified band picture can explain how the ratio (2−)/(4−) of formal oxidation numbers of zinc and of vacancy leads to the approximately one vacancy over two zinc atoms implementation ratio. Hall effect measurements indicate that the $Ba_8Zn_xGe_{46-x-y}\square_y$ deviates definitely from the Zintl rule when $0 \le x < 4$, weakly deviates when $4 \le x \le 6$, and fulfills the Zintl rule when $6 < x \le 8$. $Ba_{7.95}Zn_{7.83}Ge_{38.17}$ shows the largest power factor in our series and a ZT value at 300 K only slightly smaller than $Ba_8Ga_{16}Ge_{30}$.

Acknowledgment. The authors are indebted to Prof. Dr. Hannes Lichte for the opportunity to perform HRTEM measurements at the Triebenberg Laboratory. This work was partially supported by the FP6 Network of Excellence "Complex Metallic Alloys".

CM8028559

(47) Kuznetsov, V. L.; Kuznetsova, L. A.; Kaliazin, A. E.; Rowe, D. M. *J. Appl. Phys.* **2000**, *87*, 7871–7875.